

# Quantifying Implantation Damage and Point Defects with Multislice Electron Ptychography

Junghwa Kim<sup>1†</sup>, Colin Gilgenbach<sup>1†</sup>, Aaditya Bhat<sup>1</sup>, James LeBeau<sup>1</sup>

<sup>1\*</sup>Department of Materials Science & Engineering, Massachusetts Institute of Technology, Cambridge, 02139, Massachusetts, United States.

Contributing authors: [kjunghwa@mit.edu](mailto:kjunghwa@mit.edu); [hexane@mit.edu](mailto:hexane@mit.edu); [aadibhat@mit.edu](mailto:aadibhat@mit.edu); [lebeau@mit.edu](mailto:lebeau@mit.edu);

<sup>†</sup>These authors contributed equally to this work.

## Abstract

Ion implantation is widely used to dope semiconductors for electronic device fabrication, but techniques to quantify point defects and induced damage are limited. While several techniques can measure dopant concentration profiles with high accuracy, none allow for simultaneous atomic resolution structural analysis. Here, we use multislice electron ptychography to quantify the damage induced by erbium implantation in a wide band gap semiconductor 4H-SiC over a 1,000 nm<sup>3</sup> volume region. This damage extends further into the sample than expected from implantation simulations that do not consider crystallography. Further, the technique’s sensitivity to dopants and vacancies is evaluated as a function of damage. As each reconstructed analysis volume contains approximately 10<sup>5</sup> atoms, sensitivity of 10<sup>18</sup> cm<sup>-3</sup> (in the order of 10 ppm) is demonstrated in the implantation tail region. After point defect identification, the local distortions surrounding Er<sub>Si</sub> and v<sub>Si</sub> defects are quantified. These results underscore the power of multislice electron ptychography to enable the investigation of point defects as a tool to guide the fabrication of future electronic devices.

**Keywords:** multislice electron ptychography, ion implantation, silicon carbide, point defects

## Introduction

Ion implantation is an essential method for doping materials, where dopant ions are accelerated towards a target material at energies ranging from 10 keV to several MeV. As these high-energy ions travel through the target, their kinetic energy is transferred to the host via collisions that displace atoms and/or create vacancies in a collision cascade[1–3], resulting in a degradation of electronic, thermal, and optical properties[4–7]. While subsequent annealing is typically used to repair the damage, eliminate vacancies, and activate the dopants[8], optimizing implantation dose and annealing conditions often relies on Edisonian trial and error experiments. Building a theoretical framework to predict post-annealing device performance requires direct structural analysis of induced damage and defect configurations, which remains elusive.

Few experimental techniques are capable of capturing both the distribution of damage and dopants with direct atomic scale spatial resolution. Even obtaining an accurate concentration profile using mass spectrometry, for example, can be challenging or even impossible when surface topography is rough, *e.g.* after high temperature annealing[9, 10], when the implanted species are spatially non-homogeneous[11]. Thus, a method that can capture damage and measure dopant-level concentrations ( $< 10^{19}$  cm<sup>-3</sup>) of

point defects without geometric constraints would be an invaluable tool in next-generation semiconductor device development.

Although direct point defect identification has been successfully demonstrated with annular dark field (ADF) scanning transmission electron microscopy (STEM) [12–14], its applicability and reliability is severely limited in the thickness of the electron microscopy specimen due to dynamical scattering[15]. This generally limits dopant quantification to concentrations exceeding  $1 \times 10^{19} \text{ cm}^{-3}$  because the analyzed volume is typically less than  $300 \text{ nm}^3$  [16]. Moreover, in compound semiconductors containing light and heavy elements, such as gallium nitride (GaN) or silicon carbide (SiC), the light element sublattice is nearly invisible using high-angle ADF (HAADF) STEM[17]. Surface damage leads to decreased contrast, hindering accurate dopant determination [18], but removing this damage is challenging for materials that are highly resistant to wet etching, such as SiC[19]. Consequently, characterizing isolated point defects in the presence of sample imperfections using conventional ADF-STEM remains challenging.

Recently, multislice electron ptychography overcomes the previous obstacles of electron microscopy by recovering three-dimensional sample information encoded within the interference pattern of overlapped diffraction disks within a four-dimensional (4D) STEM dataset[20–22]. With atomic number dependence and spatial resolution limited by the thermal vibrations of the atoms[21], this method provides phase contrast originating from vacancies and dopants[21, 23], highlighting the technique’s potential as a near-ideal tool to probe the effects of implantation in a material while simultaneously characterizing sample’s structure with extremely high spatial resolution. Multislice ptychography overcomes the problems of projection and dynamical scattering by splitting the sample into a series of slices, onto which the three-dimensional sample information is preserved, enabling analysis volumes exceeding  $1,000 \text{ nm}^3$  [21, 23].

Among possible model implanted semiconductors to demonstrate the power of multislice electron ptychography, SiC has well-established synthesis processes, exists in a variety of polymorphs, and is widely used for power electronics and as a substrate for GaN in light-emitting diodes[24, 25]. Recently, it has also been shown to be a particularly promising material for scalable and integrated quantum applications due to its ability to host various types of spin defects created via implantation[26].

In this study, we demonstrate the power of multislice electron ptychography to quantify the effects of ion implantation on the 4H-SiC host matrix and single point defect quantification in volumes containing over  $10^5$  atoms. By analyzing the structure as a function of implantation depth, we reveal that the implantation-induced damage includes significant atomic displacements, and extends significantly further into the sample than predicted by implantation simulations that ignore crystallography. Further, we evaluate the sensitivity of this technique to dopants and vacancies as a function of damage. Substitutional erbium ( $\text{Er}_{\text{Si}}$ ) and silicon vacancies ( $\text{v}_{\text{Si}}$ ) are then located in three dimensions within the  $10^3 \text{ nm}^3$  ptychographic volumes, yielding a detection limit of  $10^{18} \text{ cm}^{-3}$ . Furthermore, we quantify local distortions surrounding each point defect type. This work highlights the unparalleled capability of multislice electron ptychography to investigate solid-state point defects at previously unattainable spatial resolutions and detection limits in the electron microscope, offering a robust framework for guiding the fabrication of future electronic devices.

## Overview of erbium implanted 4H-SiC

Among various SiC dopants, Er doping is widely used in optical devices as their telecom wavelength intra-4f-shell transitions are robust to external perturbations[27]. In addition, it provides a large atomic number difference with the host and thus serves an ideal dopant to validate the multislice electron ptychography technique. Here, Er is implanted into a 4H-SiC substrate (MTI Corporation, Richmond, CA) with an energy of 165 keV, a total dose of  $10^{14} \text{ ions/cm}^2$ , and a  $7^\circ$  off-axis implantation angle.

To analyze the effects of implantation on the substrate, a series of ptychography volumes are reconstructed from data acquired every every 10 nm along the implantation direction, starting 10 nm from the surface and ending 120 nm deep. A representative reconstructed volume at an implantation depth of 40 nm is shown in **Figure 1a**. Within the reconstruction volume, both Si and C sublattices are resolved due to the atomic number sensitivity of ptychography[21], with the non-equivalent  $h$  (quasi-hexagonal) and  $k$  (quasi-cubic) stacking order of 4H-SiC[28] indicated in **Figure 1b**.

While surface damage induced by sample preparation can hinder further quantitative analysis in conventional STEM (**Supplementary Figure 1**), the surface layers in the ptychographic reconstruction can be readily removed by subtracting the top- and bottom-most slices from the volume. For example, the

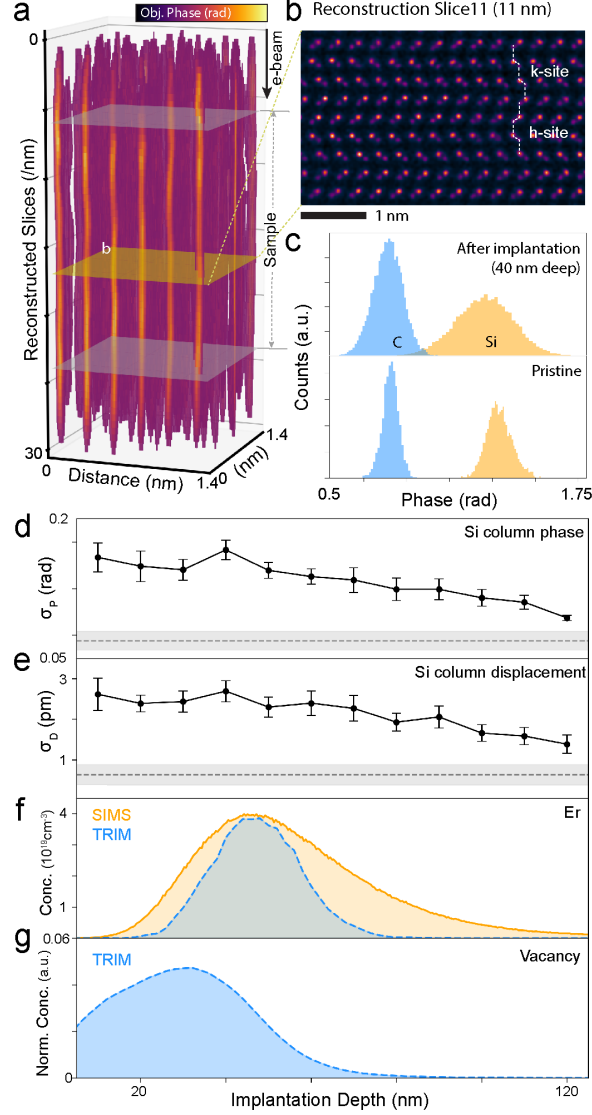


**Fig. 1 Retrieved object phases using multislice electron ptychography of Er-implanted 4H-SiC.** (a) 3D representation of Si columns along the electron beam direction, using stacked reconstructed object phase slices. (b) A reconstructed phase image of Er-implanted 4H-SiC, 11 nm below the surface of the TEM sample (reconstruction slice 11). The scale bar, 1 nm. (c) Phase distribution of Si and C sublattices in Er-implanted (top) and pristine SiC (bottom). The dataset of Er-implanted SiC was obtained from approximately 40 nm implantation depth. (d,e) Si phase variation ( $\sigma_P$ ) and Si atom displacements ( $\sigma_D$ ) over implantation depth. Dashed straight lines and shaded area in (d,e) are  $\sigma_P$  and  $\sigma_D$  measured in a pristine 4H-SiC sample. (f) Depth profile of Er ion using SIMS (orange) and TRIM calculation (blue). (g) Atomic displacement as a consequence of Er ion implantation using TRIM calculation.

standard deviation ( $\sigma$ ) of each object phase slice (**Supplementary Figure 2**), can be used to identify the abrupt decrease in object phase into reconstruction volume outside the sample.

By fitting each Si and C positions to two-dimensional Pseudo-Voigt distributions, the peak phases are extracted across the volumes at each implantation depth. The average Si peak phase gradually increases with implantation depth while the C phase remains largely constant (**Supplementary Figure 3**). As a consequence, the contrast between Si and C increases considerably from the surface to 120 nm by 22.1% (Si/C ratio  $0.92 \pm 0.05$  and  $1.13 \pm 0.13$  for 40 nm and 120 nm, respectively, **Supplementary Figure 3**). In addition, at an implantation depth of 40 nm, the measured Si and C peak phases overlap (**Figure 1c**, top panel). This contrasts with a pristine volume (without implantation) where Si always exhibit a significantly higher phase than C (Si/C ratio  $1.14 \pm 0.09$ ) with less broadening (**Figure 1c**, bottom panel).

The Si peak phase standard deviation,  $\sigma_P$ , maximum and minimum occur at implantation depths of 40 and 120 nm, respectively, as shown in **Figure 1d**. The trend is consistent with the standard deviation of the displacements of Si away from their column depth-averaged position,  $\sigma_D$ , **Figure 1e**. Notably, up to an implantation depth of 40 nm,  $\sigma_D$  is roughly constant,  $2.53 \pm 0.12$  pm, and aligns with the damage profile from TRIM calculations (**Figure 1g**). Over the next 80 nm of implantation depth,  $\sigma_D$  gradually decreases to 1.38 pm, contrasting with the damage extent predicted by naive TRIM calculations. Along low-index zones, channeling is known to increase implantation depth compared to an amorphous model [29]. Moreover, at an implantation depth of 120 nm,  $\sigma_D$  and  $\sigma_P$  remain above that of a pristine SiC, which are 0.95 pm ( $\pm 0.2$  pm) and 0.088 rad ( $\pm 0.020$  rad), respectively.

Several factors contribute to the increased displacements and subsequent broadening of the Si/C phase distribution in the implanted sample, including the presence of Er and static atomic displacements along the beam direction due to implantation damage. For the given experimental implantation conditions, naive (ignoring crystallography) Transport of Ions in Matter (TRIM) simulations predict that the maximum Er ion concentration is on the order of  $4 \times 10^{19}$  ions/cm<sup>3</sup> at an implantation depth of  $\sim 45$  nm and a penetration range up to  $\sim 100$  nm (**Figure 1f**, light blue). Simultaneously, vacancy creation is expected in the vicinity of the surface due to atomic Si and C displacements, with the highest probability at roughly 32 nm from the implantation surface (**Figure 1g**, light blue).

## Damage visualization and quantification

The three-dimensional ptychography reconstructions enables displacements to be visualized along the atom columns, as shown in **Supplementary Video 1 and 2** for implantation depths of 40 and 120 nm. Two randomly selected and representative Si atom columns and their displacements away from the column depth-average (dashed line) are shown in **Figure 2a** at the corresponding implantation depths. For the 40 nm deep case, Si exhibits significant  $xy$ -plane displacements up to approximately 20 pm, while at 120 nm, a maximum displacement of 10 pm is observed, or half that at a depth of 40 nm. Viewed along the atom columns, the displacement magnitude and angle for 10 columns at each implantation depth (**Figure 2b**) and distribution of all displacements (**Figure 2c**), show near isotropic distributions in each case. Moreover, for the C sublattice, higher displacement magnitudes are observed compared to Si (**Supplementary Figure 4**), likely due to the lower displacement threshold of C compared to Si [30].

To gain quantitative insights into the local structure of as-implanted 4H-SiC, the projected pair distribution function (pPDF) from the spacing between atom columns is calculated [31]. The pPDFs at the indicated implantation depths are shown in **Figure 2d**, while the entire series is shown in **Supplementary Figure 5**. The distances between first and second nearest like-neighbors (NLN), Si-Si or C-C, are slightly larger on average and exhibit higher scatter at an implantation depth of 40 nm compared to 120 nm. Specifically, the full-width at half-maximum (FWHM) for the first and second NLN distances of Si at 40 nm deep are 12.91 pm and 14.84 pm, respectively, whereas they are 10.35 pm and 11.27 pm at 120 nm.

In addition, the FWHM of the nearest neighbor distance, Si-C, at 40 nm is 12.04 pm, which is 20% larger than at an implantation depth of 120 nm. As previous studies have demonstrated, severely damaged and amorphized SiC can show a peak in the radial distribution function from electron diffraction at an interatomic distance of 145 pm [32, 33], which corresponds to the equilibrium bond length of C-C. Thus, the ptychography measured pPDFs (**Figure 2d**) show that the structure is not yet amorphized in the analyzed regions, with no evidence of C-C bond formation at this implantation dose. These measurements highlight the sensitivity of ptychography to quantify implantation-induced damage, which introduces measurable crystallographic disorder at the short- and medium-range length scales [34].

## Point defect detection

In addition to damage, ptychography is also sensitive to the presence of point defects [21, 23]. For the ideal case without damage-induced displacements, ptychography reconstructions using simulated 4D STEM data containing substitutional Er ( $\text{Er}_{\text{Si}}$ ) dopants show a significantly increased phase (by 18.5%) at the position of the dopants (**Figure 3a**). Unlike conventional HAADF STEM imaging with the same convergence semi-angle as experiment (**Supplementary Figure 6**), the phase and 3D positional

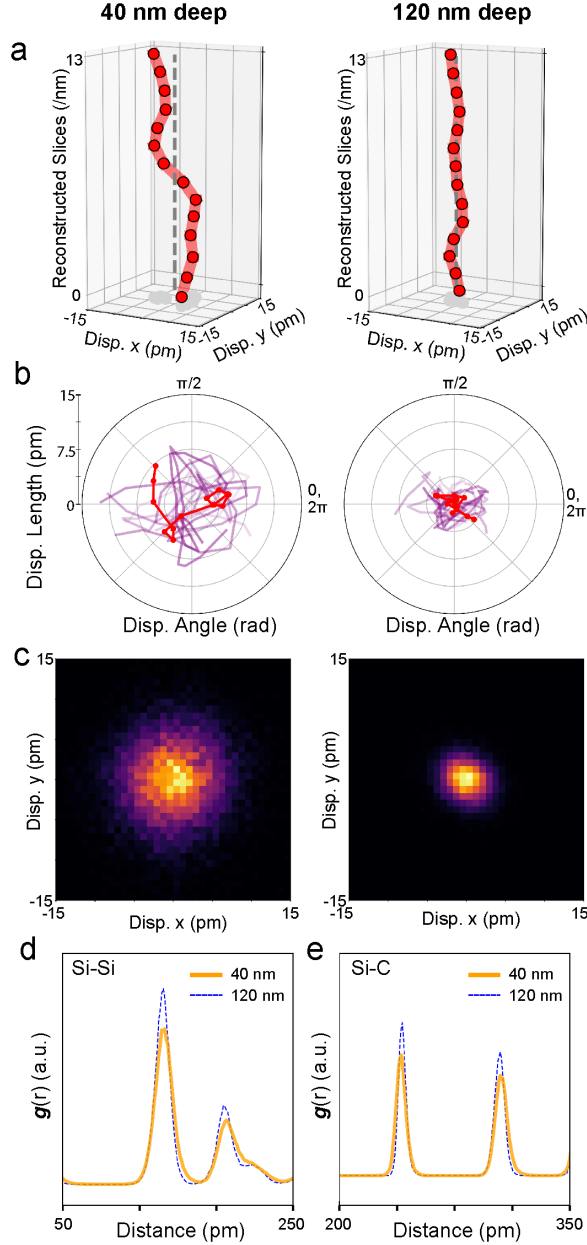


**Fig. 2 Quantification of implantation damage using multislice electron ptychography.** (a-c) Atomic displacement mapping obtained at 40 nm (left) and 120 nm implantation depth (right). (a) 3D representations of randomly chosen Si columns, with gray dotted lines indicating the depth-averaged position of each column. (b) Polar plots showing displacement magnitude and angle, highlighting their alignments along the electron beam. Displacements are analyzed from randomly selected 10 atom columns over reconstruction slices. (c) 2D maps of atomic displacement. (d,e) pPDF for Si-Si (d) and Si-C distances (e) at 40 nm (orange solid line) and 120 nm (blue dashed line) from the implantation surface.

sensitivity extends to sample thickness greater than 15 nm. Moreover, the accuracy of locating the dopant along the beam direction is 1.41 nm.

One possible  $\text{Er}_{\text{Si}}$  is marked in **Figure 3b** (blue triangle). At this position, a significant phase increase of 20.9% is observed compared to the average Si phase within the object slice. The maximum object phase occurs near the middle of this column along the  $z$ -direction, at the object slice that is 8 nm from the surface of the reconstructed volume, suggesting the presence of Er at an implantation depth of 120 nm and in agreement with SIMS.

Although the identified position in **Figure 3b** exhibits a large change in peak phase compared to the slices after, the influence of atomic displacements on phase contrast must be considered as discussed

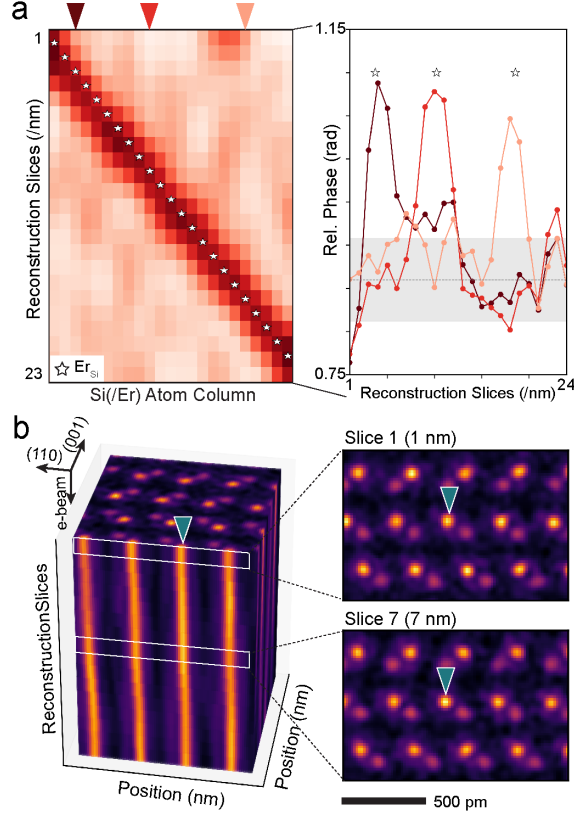


**Fig. 3 Potential point defects based on the phase contrast in reconstructed slices.** (a) Si object phases over depth through Si lattices, each containing an  $\text{Er}_{\text{Si}}$  in a 23 nm thick model. Overlaid star marks represent detected  $\text{Er}_{\text{Si}}$  and their 3D positions. Line profiles to the right show Si phases over reconstruction slices according to the atom columns denoted by triangular marks in (a). (b) 3D representation of object phases along the electron beam direction, using stacked reconstructed object phase slices obtained at 120 nm implantation depth. Right insets are reconstructed slices of the 1<sup>st</sup> and 7<sup>th</sup> slices (1 and 7 nm deep from the TEM surface, respectively). Scale bar, 500 pm.

above. Simulating 4D-STEM data and subsequent ptychography reconstructions, structural models incorporated various levels of static displacements observed above as a function of implantation depth show that these damage-induced displacements broaden the Si peak phases (**Supplementary Figure 7**) due to modified scattering along a column based on the misaligned atomic potential.

When  $\text{Er}_{\text{Si}}$  is added to the structure model with displacements (**Supplementary Figure 8**), implantation damage will also increase the spread of the  $\text{Er}_{\text{Si}}$  peak phase and leads to overlap with Si at high displacements (over  $\sigma_{\text{D}} = 1.8$  pm). As a consequence, unambiguous identification of Er becomes impossible with large static displacements in the structure, such as above an implantation depth of more than 90 nm where  $\sigma_{\text{D}}$  falls below this threshold. As a consequence, point defect detection is only considered in these deeper regions.

To determine the spatial distribution of point defects, first, we identified a suitable probability distribution that represents our experimental phase distribution from ptychography reconstruction. Given that displacement-induced misalignment and vacancies lead to decreased phase contrast, a skew-normal distribution provides an appropriate description of the data, as validated using a quantile-quantile plot (**Figure 4a**). Quantitatively, using the Kolmogorov–Smirnov test, the p-value when assuming a skew-normal distribution is 0.077, ranging from 0.047 to 0.3 over all datasets. If the distribution is modeled as Gaussian, however, the p-value is  $10^{-13}$ , and all datasets have a similarly small value. This indicates that the skew-normal distribution is a better representation of the experimental data.

The object phase along atom columns selected using this outlier measurement are shown in **Figure 4c,d** for  $\text{Er}_{\text{Si}}$  and  $v_{\text{Si}}$  respectively. Those atom columns identified to contain Er (**Figure 4c**) show a significantly higher peak phase than the Er threshold compared to the other columns. For  $v_{\text{Si}}$  containing columns (**Figure 4d**), the minimum phase dips below the vacancy threshold. Moreover, for the pristine sample using the same thresholds, no dopant candidates are detected in multiple reconstructed volumes.

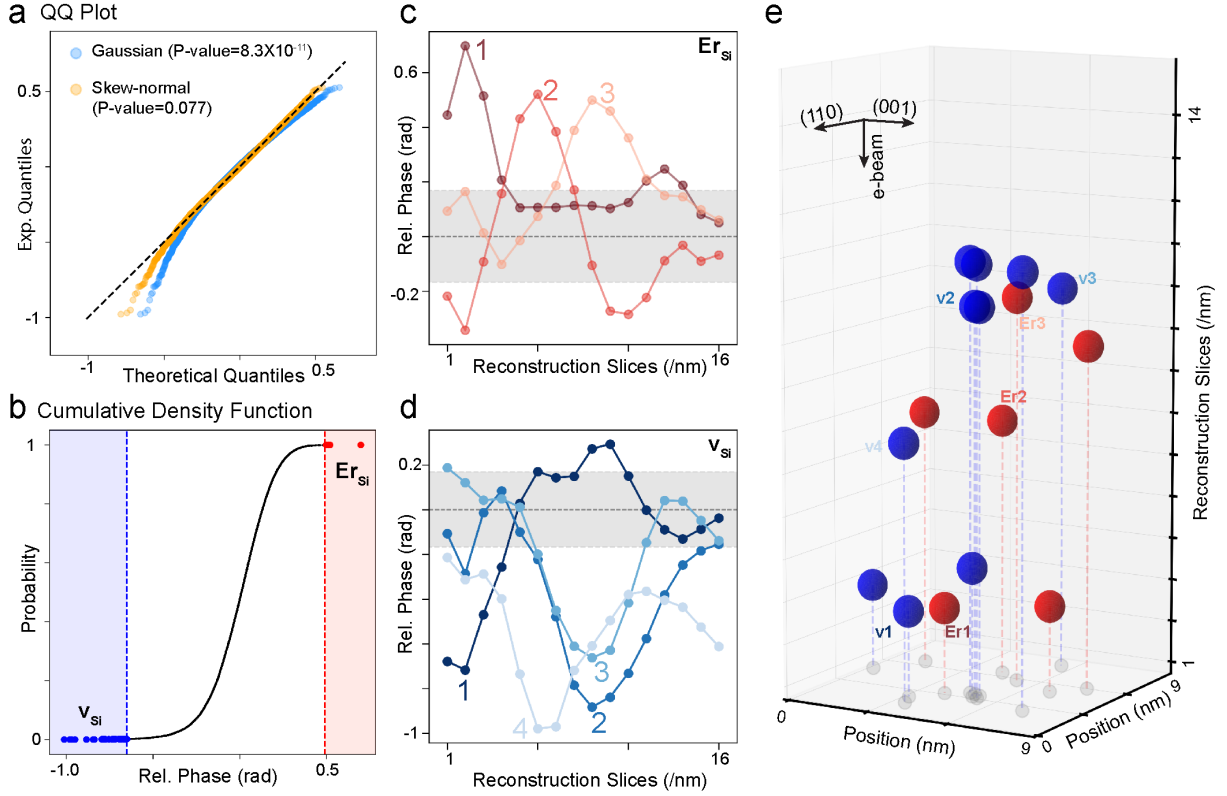


**Fig. 4 Identification of point defects and their spatial distribution in three dimensions in Er-implanted unannealed 4H-SiC.** (a) Quantile-quantile (QQ) plot of Si phase distribution obtained at a 100 nm implantation depth, compared with the Gaussian (blue) and the skew-normal distribution (orange). (b) Cumulative density function of the experimental Si phase distribution, with cutoffs for  $\text{Er}_{\text{Si}}$  (red) and  $\text{v}_{\text{Si}}$  (blue) estimated using Er profile from SIMS. (c,d) Isolated atom columns based on the cutoffs in (b), corresponding to likely  $\text{Er}_{\text{Si}}$  (c) and  $\text{v}_{\text{Si}}$  (d), respectively. Gray shaded regions represent Si phase within  $1\sigma_{\text{P}}$ , and the gray plot is an example phase profile over reconstruction layers at an atom column without point defects. (e) 3D distribution of  $\text{Er}_{\text{Si}}$  and  $\text{v}_{\text{Si}}$  within the measured volume of multislice electron ptychography, which is  $8.9 \text{ nm} \times 8.9 \text{ nm} \times 16 \text{ nm}$ .

An example reconstructed volume indicating the locations of all identified point defects is shown in **Figure 4e**, while the object phases along the atom columns containing these defects are shown in **Figure 4c** and **d**. Additional datasets at implantation depths below 90 nm are reported in **Supplementary Figure 9**. Notably, and contrary to the naive TRIM predictions where the penetration depth is approximately 100 nm (blue line in **Figure 1g**), the ptychography reconstructions detect Er at an implantation depth of around 120 nm (**Supplementary Figure 9d**). Moreover, for the reconstructed volume containing  $10^5$  atoms, the concentration of  $\text{Er}_{\text{Si}}$  detected is approximately  $2 \times 10^{18} \text{ cm}^{-3}$  ( $\sim 40 \text{ ppm}$ , ranging from  $1.6$  to  $2.1 \times 10^{18} \text{ cm}^{-3}$  considering a sample thickness  $\pm 2 \text{ nm}$ ) and is in excellent agreement with SIMS ( $2.37 \times 10^{18} \text{ cm}^{-3}$ ) at this implantation depth.

Given the field-of-view and sample thickness, a detection limit of  $10^{18} \text{ cm}^{-3}$  is attained. Further, this also contrasts with conventional elemental analysis methods in electron microscopy, such as energy-dispersive X-ray spectroscopy (EDS) and electron energy loss spectroscopy (EELS), which typically have higher detection limits, usually beyond  $10^{19} \text{ cm}^{-3}$ [35, 36]. Thus, multislice electron ptychography can achieve a level of point defect characterization unachievable with other analytical methods in the electron microscope[16].

## Point defect structure quantification

In contrast to other analytical techniques, ptychography also enables access to the local structure surrounding the point defects. To compare the structure of each defect type, the class average of  $0.8 \times 0.8 \text{ nm}^2$  patches around Si,  $\text{Er}_{\text{Si}}$ , and  $\text{v}_{\text{Si}}$  are considered. The Si class members were selected from those

within  $1\sigma_{\text{P}}^{\text{Si}}$  from the average Si phase. The 3D phase profiles of each defect class average, compared to the Si class average, are shown in **Figure 5b**, bottom panels.

Comparing the defect object phase to Si,  $v_{\text{Si}}$  exhibits a decreased phase by 0.2 rad, while  $\text{Er}_{\text{Si}}$  shows an increased phase by 0.2 rad. The phase difference corresponds to a 16% decrease compared to the average Si column, agreeing with the contrast from the simulation in **Figure 3a**. Moreover, the inequivalent hexagonal-like ( $h$ ) and cubic-like ( $k$ ) environments of Si or C sites can be separately considered, as shown in **Supplementary Figure 10**) for  $v_{\text{Si}}$  and  $\text{Er}_{\text{Si}}$ . At the  $k$ - and  $h$ -sites, 38 and 34  $v_{\text{Si}}$  are found for each, while 16 and 13 are found for  $\text{Er}_{\text{Si}}$  respectively (**Supplementary Figure 10**). The nearly equal distribution between these two sites is expected due to similar defect formation energy[37].

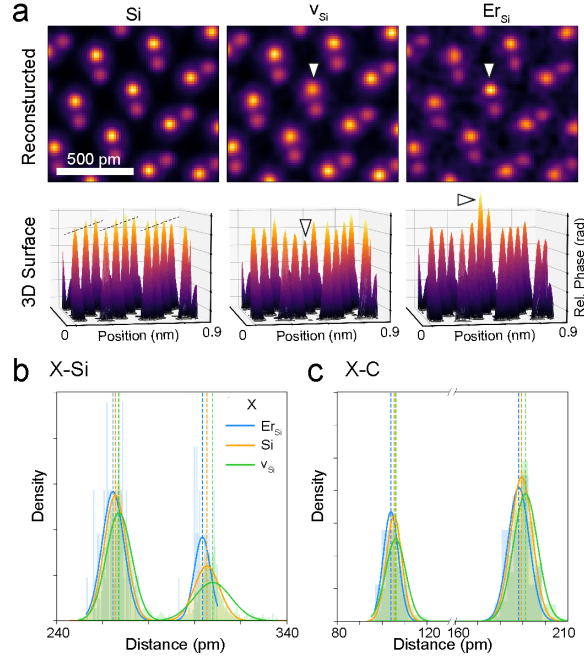


**Fig. 5** Local structures in the vicinity of point defects in Er-implanted 4H-SiC using multislice electron ptychography. (a) Cross-correlated images of pristine Si,  $v_{\text{Si}}$ , and  $\text{Er}_{\text{Si}}$  (left to right), with bottom panels showing 3D surface maps. Scale bar, 500 pm. (b,c) Distribution of bond lengths in the vicinity of  $\text{Er}_{\text{Si}}$  (blue), Si (orange), and  $v_{\text{Si}}$  (green) with neighboring Si (b) and C (c) using multislice electron ptychography.

The distances between the Si NLN at  $v_{\text{Si}}$  defects exhibit expansion of 0.6 % (with standard error of 0.06 %) to its nearest Si neighbor, which can be related to the outward relaxation due to the localization of C dangling bonds[38]. For the C NLNs, expansion is also observed at  $v_{\text{Si}}$ . This observation, coupled with the skewed distribution of the pPDF, as shown in **Figure 2f**, suggests that the lattice damage is attributable to the accumulation of vacancies, a consequence of implantation-induced damage.

## Conclusions

These results demonstrate that multislice electron ptychography enables three-dimensional quantification of atomic displacements induced from implantation. Using outlier detection based on a measured SIMS concentration profile, the distribution of both  $v_{\text{Si}}$  and  $\text{Er}_{\text{Si}}$  point defects can be identified with at a detection limit of  $10^{18} \text{ cm}^{-3}$  (10 ppm) in the electron microscope. In addition, the approach also provides detailed structural insights that can enable the correlation of processing parameters with point defects and their local structure, at concentrations relevant to semiconductor manufacturing. Overall, these findings address the long-standing need to directly characterize the structural consequences of ion implantation, *e.g.* host lattice damage or local structure surrounding point defects, and can help overcome the limitations of relying on largely empirical approaches to optimize device performance.

# Acknowledgements

The authors acknowledge support from the Air Force Office of Scientific Research (FA9550-22-1-0370). This work was performed with the assistance of MIT SuperCloud and was carried out in part through the use of MIT’s Characterization.nano facilities.

## 1 Methods

### 1.1 Sample preparation

4H-SiC samples were implanted with Er by CuttingEdge Ions (Anaheim, CA), using an incident angle that was  $7^\circ$  off the [0001] crystallographic direction and with the substrate held at  $500^\circ\text{C}$ . Er ions were implanted with an energy of 165 keV energy and a dose of  $10^{14}$  ions/cm<sup>2</sup>.

Samples for electron microscopy were prepared using the wedge polishing method[39]. This was followed by Ar ion milling from 2 to 0.3 keV to achieve thickness necessary for ptychography and minimal surface damage. Samples were baked at  $100^\circ\text{C}$  under vacuum and plasma cleaned prior to imaging to reduce contamination.

### 1.2 Data acquisition

The acquisition of HAADF and 4D-STEM datasets was conducted using a Thermo Fisher Scientific Themis Z scanning/transmission electron microscope. HAADF images were acquired with a convergence angle of 18.9 mrad, a collection angle of 65-200 mrad, and dwell time of 1  $\mu\text{s}$ /pixel.

4D-STEM datasets were collected using a  $128 \times 128$  pixel EMPAD (electron microscope pixel array detector) [40]. Datasets were collected with a dose of  $3.24 \times 10^5$  e<sup>-</sup>/Å<sup>2</sup>, a scan step size of 0.44 Å/px, a diffraction pixel size of 0.78 mrad/px, and an overfocus of 5 nm.

The sample thickness in the analyzed regions was approximately 18 nm, determined using position-averaged convergent beam electron diffraction (PACBED) analysis [41]. To investigate the distribution of dopants resulting from ion implantation, holes were drilled by the electron beam at intervals of every 10 nm from the surface along the [0001] direction, employing a high electron probe current ( $\approx 1$  nA). All STEM datasets were collected at an acceleration voltage of 200 kV.

### 1.3 Multislice simulation

Simulated 4D-STEM datasets were generated using a custom, Python-based multislice simulation package based on the algorithm described in Ref. [42]. For the simulations, supercells of 4H-SiC were created using a custom Python-based script, both with and without point defects. For those with point defects, substitutional Er<sub>Si</sub> and Si vacancies were introduced randomly within the lattice at various concentrations. Two supercells were considered. One with  $5.3 \text{ nm} \times 5.3 \times 12 \text{ nm}$  and the other  $5.3 \text{ nm} \times 5.3 \times 24 \text{ nm}$ .

All simulations were carried out with a beam energy of 200 keV, a convergence angle of 19.2 mrad, and a probe overfocus of 10 nm. To accommodate the effective source size of the probe, a 0.8 Å full-width half-maximum (FWHM) Gaussian distribution was applied with random displacements of probe positions for each thermal configuration (a total of 50 thermal configurations). The simulated data has a scan step size of 0.42 Å/px and a diffraction pixel size of 0.98 mrad/px.

### 1.4 Multislice electron ptychography reconstruction

Data processing was carried out in part using the cSAXS ptychography MATLAB package developed by the Science IT and the coherent X-ray scattering (CXS) groups, Paul Scherrer Institute, Switzerland. The version of this package used contains modifications and improvements by Zhen Chen, Yi Jiang,[21] as well as the authors. The reconstruction involved 1 nm thick object slices with 40 slices for both simulation and experiment datasets. In the process, 8 incoherent probe modes were utilized. To enhance real-space resolution, diffraction patterns were padded from  $128 \times 128$  to  $256 \times 256$  pixels.

## References

- [1] Gentils, A., Linez, F., CanizarR̄s, A., Simon, P., ThomÚ, L., Barthe, M.-F.: Influence of ion energy on damage induced by Au-ion implantation in silicon carbide single crystals. *Journal of materials science* **46**, 6390–6395 (2011)
- [2] Morehead, F., Crowder, B., Title, R.: Formation of amorphous silicon by ion bombardment as a function of ion, temperature, and dose. *Journal of Applied Physics* **43**(3), 1112–1118 (1972)
- [3] McHargue, C.J., Williams, J.: Ion implantation effects in silicon carbide. *Nuclear Instruments and Methods in Physics Research Section B: Beam Interactions with Materials and Atoms* **80**, 889–894 (1993)
- [4] Kumar, P., Martins, M.I.M., Bathen, M.E., Prokscha, T., Grossner, U.: Al-implantation induced damage in 4h-sic. *Materials Science in Semiconductor Processing* **174**, 108241 (2024)
- [5] Wood, B.S., Khaja, F.A., Colombeau, B.P., Sun, S., Waite, A., Jin, M., Chen, H., Chan, O., Thanigaivelan, T., Pradhan, N., *et al.*: Fin doping by hot implant for 14nm finfet technology and beyond. *ECS Transactions* **58**(9), 249 (2013)
- [6] Reza, A., Yu, H., Mizohata, K., Hofmann, F.: Thermal diffusivity degradation and point defect density in self-ion implanted tungsten. *Acta Materialia* **193**, 270–279 (2020)
- [7] Piluso, N., Stefano, M.A., Lorenti, S., La Via, F.: 4h-sic defects evolution by thermal processes. In: *Materials Science Forum*, vol. 897, pp. 181–184 (2017). Trans Tech Publ
- [8] Zhang, Y., Sachan, R., Pakarinen, O.H., Chisholm, M.F., Liu, P., Xue, H., Weber, W.J.: Ionization-induced annealing of pre-existing defects in silicon carbide. *Nature communications* **6**(1), 8049 (2015)
- [9] Capano, M., Ryu, S., Cooper, J., Melloch, M., Rottner, K., Karlsson, S., Nordell, N., Powell, A., Walker, D.: Surface roughening in ion implanted 4h-silicon carbide. *Journal of Electronic Materials* **28**, 214–218 (1999)
- [10] Herner, S., Gila, B., Jones, K., Gossmann, H.-J., Poate, J., Luftman, H.: Surface roughness-induced artifacts in secondary ion mass spectrometry depth profiling and a simple technique to smooth the surface. *Journal of Vacuum Science & Technology B: Microelectronics and Nanometer Structures Processing, Measurement, and Phenomena* **14**(6), 3593–3595 (1996)
- [11] Lockyer, N.P., Aoyagi, S., Fletcher, J.S., Gilmore, I.S., Heide, P.A., Moore, K.L., Tyler, B.J., Weng, L.-T.: Secondary ion mass spectrometry. *Nature Reviews Methods Primers* **4**(1), 32 (2024)
- [12] Saito, G., Yamaki, F., Kunisada, Y., Sakaguchi, N., Akiyama, T.: Three-dimensional analysis of eu dopant atoms in ca- $\alpha$ -sialon via through-focus haadf-stem imaging. *Ultramicroscopy* **175**, 97–104 (2017)
- [13] Ishikawa, R., Lupini, A.R., Findlay, S.D., Taniguchi, T., Pennycook, S.J.: Three-dimensional location of a single dopant with atomic precision by aberration-corrected scanning transmission electron microscopy. *Nano letters* **14**(4), 1903–1908 (2014)
- [14] Ishikawa, R., Lupini, A.R., Findlay, S.D., Taniguchi, T., Pennycook, S.J.: Three-dimensional location of a single dopant with atomic precision by aberration-corrected scanning transmission electron microscopy. *Nano letters* **14**(4), 1903–1908 (2014)
- [15] Bosch, E.G., Lazić, I.: Analysis of depth-sectioning stem for thick samples and 3d imaging. *Ultramicroscopy* **207**, 112831 (2019)
- [16] Ishikawa, R., Shibata, N., Taniguchi, T., Ikuhara, Y.: Three-dimensional imaging of a single dopant

- in a crystal. *Physical Review Applied* **13**(3), 034064 (2020)
- [17] Lin, Y., Chen, L., Hsieh, C., Chang, M., Fung, K., Hu, A., Lo, S., Chen, F., Kai, J.: Atomic configuration of point defect clusters in ion-irradiated silicon carbide. *Scientific Reports* **7**(1), 14635 (2017)
- [18] Yamazaki, T., Watanabe, K., Nakanishi, N., Hashimoto, I.: Role of surface amorphous film in high-resolution high-angle annular dark field stem imaging. *Ultramicroscopy* **99**(2-3), 125–135 (2004)
- [19] Isohashi, A., Bui, P., Toh, D., Matsuyama, S., Sano, Y., Inagaki, K., Morikawa, Y., Yamauchi, K.: Chemical etching of silicon carbide in pure water by using platinum catalyst. *Applied Physics Letters* **110**(20) (2017)
- [20] Gao, S., Wang, P., Zhang, F., Martinez, G.T., Nellist, P.D., Pan, X., Kirkland, A.I.: Electron ptychographic microscopy for three-dimensional imaging. *Nature communications* **8**(1), 163 (2017)
- [21] Chen, Z., Jiang, Y., Shao, Y.-T., Holtz, M.E., Odstrčil, M., Guizar-Sicairos, M., Hanke, I., Ganschow, S., Schlom, D.G., Muller, D.A.: Electron ptychography achieves atomic-resolution limits set by lattice vibrations. *Science* **372**(6544), 826–831 (2021)
- [22] Sha, H., Cui, J., Li, J., Zhang, Y., Yang, W., Li, Y., Yu, R.: Ptychographic measurements of varying size and shape along zeolite channels. *Science Advances* **9**(11), 1151 (2023)
- [23] Dong, Z., Huo, M., Li, J., Li, J., Li, P., Sun, H., Lu, Y., Wang, M., Wang, Y., Chen, Z.: Visualization of oxygen vacancies and self-doped ligand holes in  $\text{La}_3\text{Ni}_2\text{O}_7$ . arXiv preprint arXiv:2312.15727 (2023)
- [24] Elasser, A., Chow, T.P.: Silicon carbide benefits and advantages for power electronics circuits and systems. *Proceedings of the IEEE* **90**(6), 969–986 (2002)
- [25] Edmond, J., Abare, A., Bergman, M., Bharathan, J., Bunker, K.L., Emerson, D., Haberern, K., Ibbetson, J., Leung, M., Russel, P., *et al.*: High efficiency gan-based leds and lasers on sic. *Journal of Crystal Growth* **272**(1-4), 242–250 (2004)
- [26] Son, N.T., Anderson, C.P., Bourassa, A., Miao, K.C., Babin, C., Widmann, M., Niethammer, M., Ul Hassan, J., Morioka, N., Ivanov, I.G., *et al.*: Developing silicon carbide for quantum spintronics. *Applied Physics Letters* **116**(19) (2020)
- [27] Parker, R., Dontschuk, N., Sato, S.-I., Lew, C.-K., Reineck, P., Nadarajah, A., Ohshima, T., Gibson, B., Castelletto, S., McCallum, J., *et al.*: Infrared erbium photoluminescence enhancement in silicon carbide nano-pillars. *Journal of Applied Physics* **130**(14) (2021)
- [28] Jepps, N., Page, T.: Polytypic transformations in silicon carbide. *Progress in crystal growth and characterization* **7**(1-4), 259–307 (1983)
- [29] Nordlund, K., Djurabekova, F., Hobler, G.: Large fraction of crystal directions leads to ion channeling. *Physical Review B* **94**(21), 214109 (2016)
- [30] Meyer, J.C., Eder, F., Kurasch, S., Skakalova, V., Kotakoski, J., Park, H.J., Roth, S., Chuvilin, A., Eyhusen, S., Benner, G., *et al.*: Accurate measurement of electron beam induced displacement cross sections for single-layer graphene. *Physical review letters* **108**(19), 196102 (2012)
- [31] Sang, X., LeBeau, J.M.: Revolving scanning transmission electron microscopy: Correcting sample drift distortion without prior knowledge. *Ultramicroscopy* **138**, 28–35 (2014)
- [32] Ishimaru, M., Bae, I.-T., Hirotsu, Y., Matsumura, S., Sickafus, K.E.: Structural relaxation of amorphous silicon carbide. *Physical review letters* **89**(5), 055502 (2002)

- [33] Fan, Y., Xu, Z., Song, Y., Sun, T.: Molecular dynamics simulation of silicon vacancy defects in silicon carbide by hydrogen ion implantation and subsequent annealing. *Diamond and Related Materials* **119**, 108595 (2021)
- [34] Sprouster, D.J., Snead, L.L., Dooryhee, E., Ghose, S.K., Koyanagi, T., Katoh, Y.: Pair distribution function analysis of neutron-irradiated silicon carbide. *Journal of Nuclear Materials* **527**, 151798 (2019)
- [35] Nasrazadani, S., Hassani, S.: Modern analytical techniques in failure analysis of aerospace, chemical, and oil and gas industries. *Handbook of materials failure analysis with case studies from the oil and gas industry*, 39–54 (2016)
- [36] Servanton, G., Pantel, R.: Arsenic dopant mapping in state-of-the-art semiconductor devices using electron energy-loss spectroscopy. *Micron* **41**(2), 118–122 (2010)
- [37] Bockstedte, M., Mattausch, A., Pankratov, O.: Ab initio study of the migration of intrinsic defects in 3C-SiC. *Physical Review B* **68**(20), 205201 (2003)
- [38] Zywietz, A., Furthmüller, J., Bechstedt, F.: Vacancies in sic: Influence of jahn-teller distortions, spin effects, and crystal structure. *Physical Review B* **59**(23), 15166 (1999)
- [39] Voyles, P.M., Grazul, J.L., Muller, D.A.: Imaging individual atoms inside crystals with ADF-STEM. *Ultramicroscopy* **96**(3-4), 251–273 (2003)
- [40] Tate, M.W., Purohit, P., Chamberlain, D., Nguyen, K.X., Hovden, R., Chang, C.S., Deb, P., Turgut, E., Heron, J.T., Schlom, D.G., *et al.*: High dynamic range pixel array detector for scanning transmission electron microscopy. *Microscopy and Microanalysis* **22**(1), 237–249 (2016)
- [41] LeBeau, J.M., Findlay, S.D., Allen, L.J., Stemmer, S.: Position averaged convergent beam electron diffraction: Theory and applications. *Ultramicroscopy* **110**(2), 118–125 (2010)
- [42] Kirkland, E.: *Advanced computing in electron microscopy* (2010). URL <http://books.google.com/books>